Improved Arterial Tissue Differentiation by Spectroscopic Optical Coherence Tomography

DOI 10.17691/stm2015.7.1.02
Received October 29, 2014

© **C. Flueraru,** PhD PEng, Senior Research Officer[1];
D.P. Popescu, PhD, Associate Research Officer[2];
Y. Mao, PhD, Associate Research Officer[1];
S. Chang, PhD, Senior Research Officer[1];
M.G. Sowa, PhD, Senior Research Officer[2];
A. Vitkin, PhD M-CCPM, Senior Scientist, Division of Biophysics and Bioimaging, Ontario Cancer Institute / Princess Margaret Cancer Centre; Professor, Department of Medical Biophysics[3]

[1]Information and Communication Technology, National Research Council of Canada, 1200 Montreal Road, Ottawa, Ontario, K1G6R6, Canada;
[2]Medical Devices, National Research Council of Canada, 435 Ellice Avenue, Winnipeg, Manitoba, R3B 1Y6, Canada;
[3]University of Toronto, 610 University Avenue, Toronto, Ontario, M5G 2M9, Canada

Optical coherence tomography (OCT) is a relatively new imaging modality similar with ultrasound where the sound waves are replaced by ballistic photons. OCT provides images at high spatial resolution which allow for the identification of micron size morphological tissue structures. A high impact application is visualization of arterial wall and atherosclerotic plaques. Despite high spatial resolution to complete the transfer of this imaging modality into clinical environment there is a need for markers which would quantify the physiological condition of the sample. Finding the proper markers is a topic of high interest for many research groups. A potential marker suggested by the OCT community is the optical attenuation coefficient. Although OCT image itself provides important diagnostic and structural information there are also new methods of tissue characterization that have been developed through spectroscopic OCT and quantitative OCT. Spectroscopic OCT investigates the spectral response while the quantitative OCT extends the investigation to non-spectral parameters. Here we investigate two procedures for calculation of optical attenuation coefficient dependence versus wavelength. The wavelength analysis will provide new insight into the chemical nature of the sample, because the spectral backreflected signal depends on sample absorption and scattering properties. In this study we demonstrate the application of OCT for quantitative and spectral analysis of vulnerable plaque morphology on Watanabe heritable hyperlipidemic – myocardial infarction (WHHLMI) rabbit model. The results suggest that the spectral dependence of the derived OCT attenuation coefficient can be used for tissue differentiation. We demonstrated that differences and the spectral dependence of the optical attenuation coefficient are linked to the macrophage content of the region of interest.

Key words: optical coherence tomography; quantitative and spectral analysis; WHHLMI rabbits.

Introduction. Currently, optical coherence tomography (OCT) is the only intravascular imaging modality with spatial resolution that allows visualization of the subsurface vascular wall morphology for plaque assessment [1, 2]. Atherosclerotic lipid plaques have different compositions and morphologies with some significantly more prone to rupture or erosion of the fibrous cap than others. They are classified in five types of lesions (I–V). Amongst these, type IV lesions are known as atheromas while type V is characterized by the presence of more fibrotic tissue than type IV. It is currently believed that the IV and V types are the most risky and prone to the rupture of the fibrous cap. The purpose of imaging vulnerable plaques using OCT is the identification of three types of morphologies that relate to risk: lipid pools, fibrous caps and calcified regions. Within the arterial OCT images, the following qualitative feature identifiers were proposed in regard to these morphologies [3]: 1) calcifications within the plaque are identified by the presence of low backscattering heterogeneous regions with well-delineated boundaries, 2) fibrous tissue appears homogeneous with strong signal backscattering, and 3) lipid pools appear as regions with ill-delineated boundaries and relatively high signal attenuation. There is wide acceptance of these qualitative rules to differentiate among the aforementioned tissue morphologies [4], based on extensive comparisons between OCT and histological images [5]. It has been established that OCT has high sensitivity and specificity for characterization of plaques as validated by histological examinations. Yabushita et al. [6] performed a qualitative OCT image classification scheme using more than 300 excised human artherosclerotic arterial segments by comparing them with corresponding histology. It was concluded that OCT had a sensitivity and specificity of 71–79 and 97–98% for fibrous regions, 95–96 and 97% for fibrocalcific regions, and 90–94.5 and 90–92% for lipid-rich plaques, respectively. Other reports analyzing the optical attenuation for arterial tissue have been published [7–9].

However, despite the consensus guidelines for evaluating the plaque morphology, more parameters are

Corresponding author: Costel Flueraru, e-mail: costel.flueraru@nrc-cnrc.gc.ca

required to better differentiate and assess different tissue structures, and to further increase OCT's sensitivity and specificity.

In this paper, we describe a method to extract the spectral dependence of OCT attenuation coefficients within arterial tissue for different wavelength ranges within the bandwidth of the OCT light source. These spectroscopic OCT approaches hold promise for a more comprehensive tissue analysis and clinical differentiation. Several spectroscopic approaches have been reported [10–12], some of them complex and computer/time demanding; therefore we are suggesting here a simple and fast method with high potential for tissue differentiation.

Materials and Methods. The OCT setup used in this study has been described previously [13, 14] and it is not going to be repeated here in detail. The OCT system used in this report is based on a quadrature interferometer [15] which allows the extraction of both real and imaginary components of the complex interferometric signal [16]. We used balanced detection detectors (Thorlabs, Inc., USA) and two acquisition channels with a high speed digitizer (AlazarTech Inc., Canada) and a commercially available swept-laser source (Santec, Japan) with a 110 nm spectral range (centered around 1310 nm) and 20 kHz repetition rate. The signal reflected by the sample is amplified by a semiconductor optical amplifier (Covega, USA) before being distributed to the detection stage. Overall, the OCT system used proposed here shows an increase of the signal to noise ratio up to 7 dB at a depth of 0.5 mm, compared to a "conventional-architecture" OCT system [13].

Note that the catheter design and fabrication [17] is a critical requirement in obtaining relevant images.

Arterial tissues. Samples in this study were *ex vivo* coronary arterial tissue from Watanabe heritable hyperlipidemic – myocardial infarction (WHHLMI) rabbits [18]. WHHLMI rabbit was developed as an animal model for spontaneous myocardial infarction by serial and selective breading of the coronary atherosclerosis-prone Watanabe heritable hyperlipidemic (WHHL) rabbits [19]. WHHLMI rabbits are characterized by the high incidence of fatal myocardial infarction at relatively early ages. The histological examination [18] of arterial tissue collected from suddenly deceased ("natural", spontaneous pathology occurrence) WHHLMI rabbits exhibit severe atheromatous plaques with more than 90% lumen being stenosed and near-rupture features: thin fibrous cap with a large lipid core and calcium accumulation mixed with a large number of macrophages. These features are consistent with vulnerable plaques, but with no rupture or luminal thrombosis detected [18]. This observation is consistent with a previous report [19] showing the same (no rupture of vulnerable plaques) characteristics in the previous strain of WHHL rabbits.

For the presented study, arterial segments from several WHHLMI rabbit specimens were snap-frozen and stored at –80°C after they were harvested. In this report we used six samples of arterial tissue and imaged six to ten locations in each case. After a short period of thawing at room temperature, the arterial samples were cut open to expose their inner luminal surface to the OCT beam. The acquisition of images was conducted at room temperature. The OCT imaging catheter was used in the forward-viewing geometry (+/–1.5 mm lateral scans enabled by a galvo-scanner, as described in [13, 14, 17]).

Model for optical attenuation coefficient and its dependence on wavelength. The OCT signal is attenuated due to scattering and absorption of light within the turbid medium of the biological sample. The attenuation coefficient can be calculated by fitting the experimental A-scan with a model based on single or multiple light scattering. In a single scattering model, it is assumed that only light backscattered once contributes to the OCT signal [20]. As a further refinement, Thrane et al. [21] proposed a model of the OCT signal that considers multiple scattering. Faber et al. [22] discussed in detail single versus multiple scattering models used in the analysis of OCT signals. In the case of the single scattering model, the fit parameter is the attenuation coefficient, while in the case of the multiple scattering there were two parameters, the attenuation coefficient and the root-mean-square scattering angle. The goodness-of-fit for both models was evaluated [22] by comparing the correlation coefficient R^2 between the model prediction and the experimental A-scans. For our research, the single scattering model consistently yielded a better fit to the experimental data with higher R^2 values [9]. This finding is not surprising, since during imaging the confocal and the coherence gates were purposely overlapped (by design) in order to reduce the contribution from multiple scattering to the OCT signal. We therefore conclude that a single scattering model offers an accurate description of our OCT data and is suitable to model the OCT signals acquired in this study. In this model, the mean photo-detector current is directly related to the OCT signal generated at the corresponding depths within the sample, as described by [9, 20]:

$$i(z) \propto \sqrt{h(z)\exp(-2\mu_{att}z)}, \quad (1)$$

where $i(z)$ represents the photo-current as a function of depth z, $h(z)$ is the axial point spread function of the OCT imager and μ_{att} is the attenuation coefficient of the OCT signal.

Recently a new OCT theoretical model was suggested by Turchin et al. [23, 24] which account for multiple scattering event and uses the total scattering coefficient, backscattering probability and the variance of a small-angle scattering function as fitting parameters.

We have previously demonstrated that the optical attenuation coefficient can differentiate arterial tissue morphology [20]. The attenuation of the OCT signal can be calculated by using one of the following two algorithms: (i) applying the fit of Eq. (1) on each individual A-scan, then statistically processing the results over all A-scans contained within the selected region of interest (ROI), or (ii) averaging all A-scans available in the ROI followed by fitting of Eq. (1) to the compounded depth profile. Here we investigate both approaches and designate the results as fit-then-average (FTA) and average-then-fit (ATF) for the case (i) and (ii) respectively.

The backscattered signal is non-stationary with both time (space) and frequency (wavenumber) variations. The axial

resolution of an OCT image is determined by the bandwidth of the light source and maximum spatial resolution is reached by using the whole light source spectrum in calculating the depth reflectivity dependence by inverse Fourier transform. While the maximum spatial resolution is reached in this case, the spectral information is not utilized. In order to extract the depth resolved spectroscopic information using a time domain OCT system, Morgner et al. [25] has proposed a short time Fourier transform (STFT) or a continuous wavelet transform. A similar approach was proposed for Fourier domain OCT [26]. The extraction of spectral dependence of optical properties uses a time-frequency analysis. However, time-frequency uncertainty principle limits the spatial and spectral resolution, so there is an inherent trade-off between them. To overcome this, Robles et al. [27] have recently proposed a dual-window method to extract the spectroscopic information while maintaining the spatial resolution, thus bypassing the spatial-spectral compromise. Their initial findings are promising, but computationally quite complex. In this study, we thus focus on a fast, reliable and simple method that can provide the operator with an on-line, real-time evaluation of features of interest.

In this study, we used a spectral resolution of ~11 nm. This bandwidth preserves some of the main features recorded on the OCT images acquired using the full spectrum of the swept-source. The swept laser source had a bandwidth of $\Delta\lambda$=110 nm (centered around 1320 nm) which corresponds to bandwidth in k-space of Δk=0.397 μm^{-1} (centered around k_0=4.76 μm^{-1}). The selected 11 nm spectral resolution was obtained by dividing the 110 nm bandwidth of the light source in ten intervals (N=10). Therefore the spectral properties obtained are averaged over an 11 nm bandwidth. From this point, there are two options available: 1) working with the constant wavelength interval approach, i.e. selecting a wavelength interval of 11 nm or 2) using a constant wavenumber interval — selecting a spectral interval of Δk=0.0397 μm^{-1}=Δk/10. Due to the inverse proportionality relation between wavelength and wavenumber, a constant spectral interval of Δk=0.0397 μm^{-1} does not correspond to constant wavelength interval across the whole swept-source bandwidth. It is known that by selecting a constant spectral interval in the k-space (option (2)) the spatial resolution is constant for each group of B-scan images corresponding to each one of the ten spectral intervals. Therefore, the spatial resolution of an OCT image calculated for a spectral interval Δk is

$$\delta Z_R(\delta k) \geq \frac{1}{2\delta k} = \frac{N\delta Z_R}{4\sqrt{\ln 2}}, \quad (2)$$

where Δk is the spectral interval width in k-space, N is the number of spectral intervals (here N=10) the available spectral domain has been divided into, and δZ_R is the spatial resolution corresponding to the whole spectral bandwidth of light source.

The OCT system used for this study utilizes a Fourier domain swept-source engine; thus spectroscopic analysis can be done using a short-frequency Fourier transform (SFFT) which the equivalent of the STFT in the time domain. The A-scan is re-calculated to determine the spectral dependence by using a filter $w(k_n, \delta k)$ with a spectral interval width of Δk centered at k_n, k_n being the center of each spectral interval and equally distributed over the k-space associated with the source spectrum. As discussed recently [28, 29] the shape of this filter (Gaussian, smoothed rectangular and rectangular) is relevant and linked to the accuracy of the extracted spectral properties. In this work we used the rectangular filter which seems to be giving the most accurate results. The re-calculated A-scan is described by

$$i(z, k_n) = FT^{-1}\{w(k_n, \delta k) S(k) I(k)\}, \quad (3)$$

where $S(k)$ is optical power spectral density of the light source and $I(k)$ is the optical intensity on the detector.

Ten images (B-scans) are extracted, each one corresponding to a constant spectral interval (Δk=0.0397 μm^{-1}) centered at

$$k_n = k_0 + \frac{\Delta k}{N}\left(n - \frac{1}{2}\right), \text{ n=1, ..., 10,} \quad (4)$$

where k_0 is the smallest wavenumber (largest wavelength) within the light source bandwidth. For the OCT system used in this study, the spatial resolution of each spectrally separated B-scan is 19 μm (calculated with Eq. (2)). With this approach the spectral response of the sample in each of these spectral intervals has been determined at the expense of slightly reduced spatial resolution. If the spatial resolution is sufficient to distinguish regions with different known pathologies, then the reduced-resolution OCT images come with the added benefit of local optical properties (attenuation coefficient) determination.

Results and Discussion

Qualitative description of arterial tissue. The correlation between OCT and histological images are strong, as demonstrated previously [30, 31]. OCT contrast relies on changes in refractive index that modulate tissue scattering and absorption properties. Extensive OCT reports, validated by histology, were published that have identified the morphological feature specific to vulnerable plaque. The plaque features of interest are the presence and the geometrical dimension of thin fibrous cap, necrotic lipid core and the accumulation of macrophages. However the assessment of plaque by OCT remains largely qualitative, with the exception of the measurement of the thickness of the fibrous cap covering necrotic lipid areas. Recently, quantitative OCT evaluation of arterial tissue using the attenuation and the back scattering coefficients has been reported [2].

Spectroscopic attenuation coefficient analysis. Previous section presented a somewhat qualitative description of OCT images. To quantify the OCT findings, we now calculate the optical attenuation coefficient of the OCT using the single scattering model and fixed geometry by fitting the A-scan from within the selected ROI (Figure 1) with Eq. (1). The size of the ROI is 330×135 (width × depth) pixels, which corresponds to a geometrical size of 1099×567 μm^2. According to the above-mentioned guidelines for morphological interpretation of the OCT image, the selected ROI lies in a lipid pool region. Two different algorithms are investigated: (i) fit-then-average, FTA, where a fit is performed on each A-scan, followed by a statistical analysis

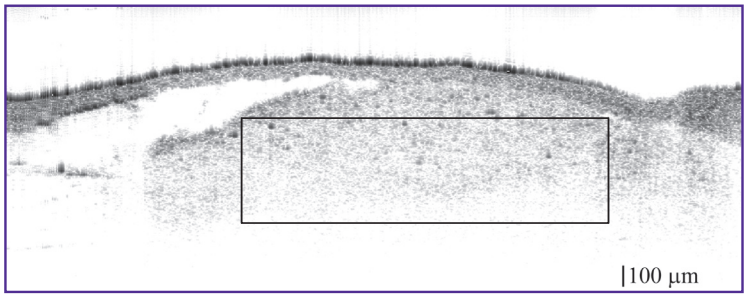

Figure 1. OCT image of arterial tissue, with a selected region of interest encompassing a large lipid accumulation

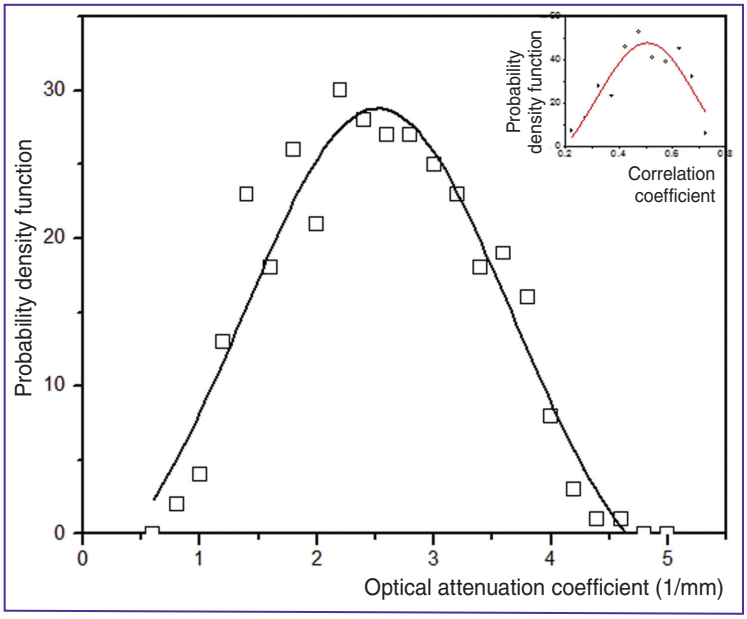

Figure 2. The Gaussian probability distribution function of the optical attenuation coefficient μ_{att} calculated by fitting Eq. (1) to each of the 330 A-scans (FTA analysis) within ROI indicated in Figure 2. Inset: the Gaussian probability distribution function of the correlation coefficient calculated between the fit and the section of A-scan part of ROI

of the individually-derived attenuation coefficients, and (ii) average-then-fit, ATF, where an average of all A-scans is followed by a fit on the averaged A-scan for attenuation coefficient extraction. There has been no reported comparison of these two algorithms in the literature. One may expect them to perform differently because of speckle — by averaging (compounding) the A-scans before fitting as per ATF algorithm (ii), a reduction of the optical speckle effects is expected, with potentially improved accuracy for attenuation coefficient determination.

FTA algorithm. For each of the 330 A-scans included in the ROI, the attenuation coefficient was calculated by fitting the profile with Eq. (1). Figure 2 displays the frequency of occurrence of the derived attenuation coefficients from the ROI shown in Figure 1. The data is fitted with a Gaussian distribution peaked at μ_{att}=2.52±1.14 mm^{-1}.

The goodness of fit is evaluated by the correlation coefficient R^2, calculated for each A-scan. The goodness of fit was modest, with R^2 values ranging from 0.23 to 0.72 (average 0.5).

ATF algorithm. In algorithm (ii), A-scans included in the ROI are first averaged; the resultant compounded profile is smoother than individual A-scans. This is a widely used approach for reducing the optical speckle effect. Figure 3 displays the compound A-scan and its corresponding fit obtained via Eq. (1). The resulting best-fit attenuation coefficient is μ_{att}=2.53±0.05 mm^{-1}. While this agree well with previous results from FTA (method (i)) analysis, the goodness of fit is now much better with R^2=0.97.

We conclude that both methods yield the same mean value for the attenuation coefficient but with large differences in standard errors and goodness of fit. The large standard deviations associated

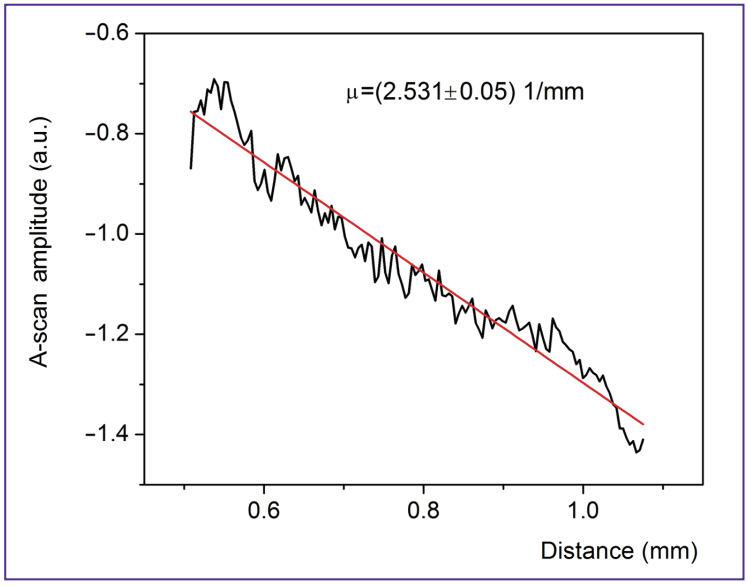

Figure 3. Compound profile obtained by averaging all A-scans within the ROI. The attenuation coefficient was calculated by fitting (ATF analysis) the obtained profile with Eq. (1)

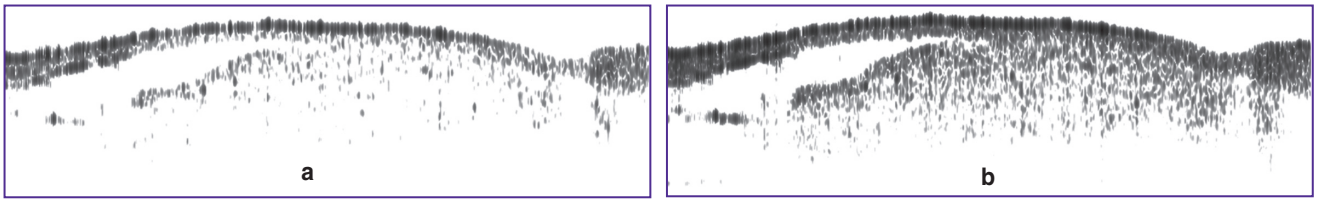

Figure 4. (a) B-scan image of an WHHLMI rabbit arterial tissue for a spectral interval of 11.5 nm centered at 1.295 μm; (b) B-scan image of an WHHLMI rabbit arterial tissue for a spectral interval of 12.8 nm centered at 1.365 μm. The corresponding OCT image acquired using the full optical spectrum of the light source is shown in Figure 2. Both images have the same size of 3.0×1.5 mm² (width × depth)

with attenuation coefficient calculation in FTA method are due to optical speckle effects.

The Gaussian distribution of the attenuation coefficient after FTA means the selected ROI is optically homogenous. In general the transition from optically homogeneous to heterogeneous ROI is gradual "real" tissue being in-between these two extremes. The level of heterogeneity can be assessed by the deviation from the Gaussian distribution of the attenuation coefficient after FTA. For this study ROIs are quasi-homogeneous with a Gaussian fit estimated by a goodness of fit (R^2) higher than 0.95.

Spectroscopic optical attenuation coefficient analysis. Using the procedure presented and employing Eq. (3), the OCT data was split into ten spectral intervals by using rectangular filters. As previously stated, the widths of the ten spectral intervals are equal in the wavenumber domain. In this way, there are ten OCT images corresponding to ten spectral domains covering the whole bandwidth available. Figure 4 (a) and (b) shows representative spectral images obtained by using the window (filter) centred at 1.295 μm with a width of 11.5 nm, and at 1.365 μm with a width of 12.8 nm respectively.

As expected, the reduced spectral width reduces the axial spatial resolution (from ~5.25 to ~19 μm) but each image contains important spectral information corresponding to the wavenumber interval used. Both images are displayed using identical image parameters (e.g., contrast and brightness). From the Figure 4 (a) and (b), it is obvious that the OCT image at 1.365 μm has a better signal-to-noise ratio at locations deeper within the artery than the image obtained at 1.295 μm.

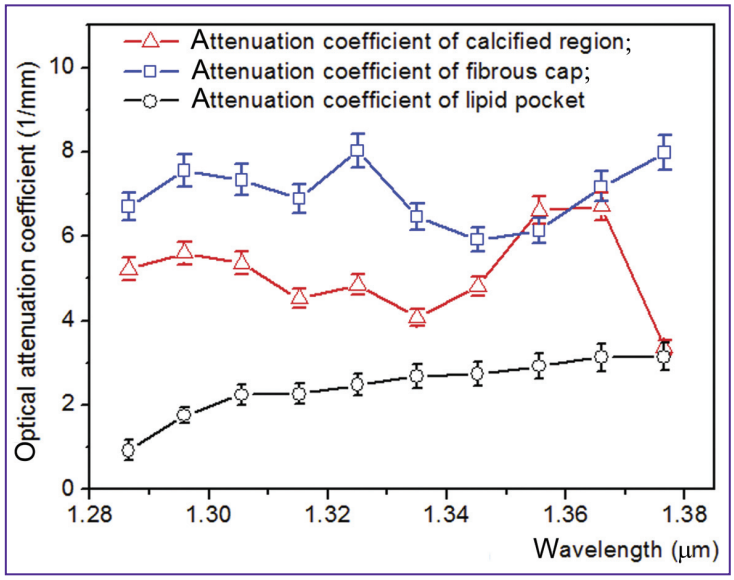

Figure 5. Optical attenuation coefficient of the OCT signal versus wavelength calculated for calcified region, fibrous cap and lipid pocket. The regression lines are guides for the eye

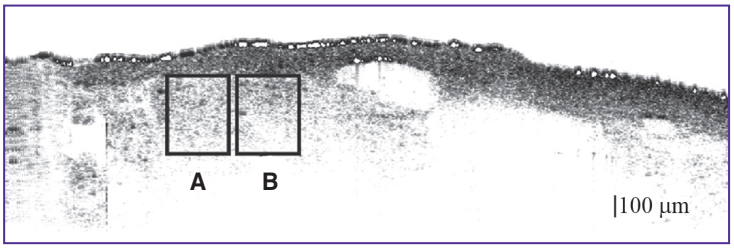

Figure 6. OCT image of atherosclerotic lesion. Two ROIs were selected; region A has a lower macrophage content than region B. ROI *A* and *B* have the same size, 243×373 μm². The image size is 3.0×1.5 mm² (width × depth)

The same qualitative guidelines and identification of different morphometric regions can be applied on each of the spectrally separated images. Therefore, by applying the attenuation model on each of these images, the dependence of the attenuation coefficient on wavelength in ten distinct spectral intervals can be extracted, potentially yielding additional useful information for arterial tissue quantification (specifically its identification and segmentation).

Following the qualitative selection of OCT image textures, we identified ROIs corresponding to lipid, calcified plaque and fibrous regions. The ATF attenuation coefficient extraction procedure was applied only for ROIs with 100 μm in depth, which is several times larger than the spatial resolution of OCT data in the spectrally separated images. Figure 5 shows the dependence of optical attenuation coefficient of the OCT signal on wavelength for calcified region, fibrous cap and lipid pool. As seen the ROI *A* and *B* in Figure 6 are part of the same qualitative feature. The dark spots visible in both ROIs are identified as macrophages. It is noticeable

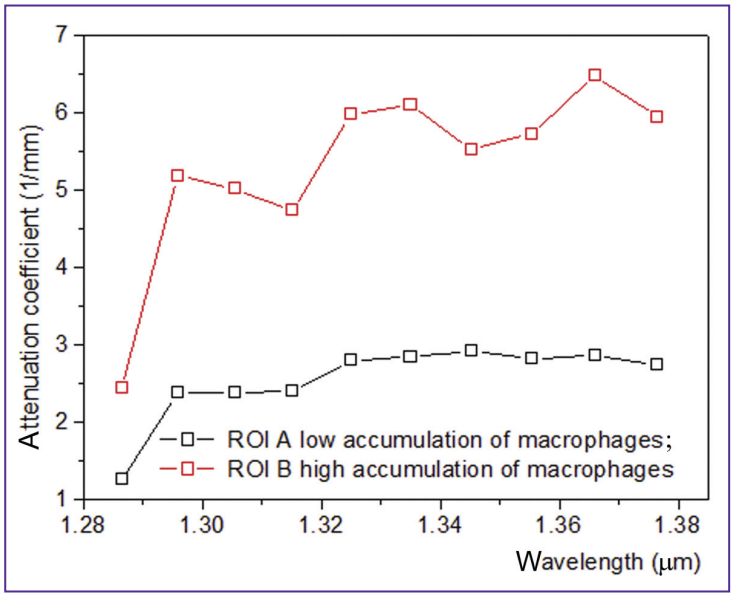

Figure 7. Optical attenuation coefficient versus wavelength for the ROIs *A* and *B*. Region *A* has a lower content of macrophages than region *B*. The regression lines are guides for the eye

that ROI *B* has a higher density of macrophages (dark spots) than ROI *A*. We have calculated the wavelength-dependent optical attenuation coefficient in ROI *A* (lower macrophages content) and ROI *B* (higher macrophage accumulation) and plot the results in Figure 7. The results show similar spectral dependence in both ROIs but more importantly reveal a higher attenuation coefficient in region *B* with its higher macrophage content. This demonstrates a simple metric to quantitatively assess tissue. Using proper calibration methodology, the increased attenuation coefficient can be linked to the density of macrophages within the selected ROI.

Conclusions. OCT is playing an increasingly significant role in the quest to understand and manage vulnerable plaque. We used a patented swept-source optical coherence tomography system [16] with optical amplification to image *ex vivo* arterial tissues with known pathology, using a WHHLMI rabbit model. Using comparisons between histological and OCT images, we confirmed the recently proposed qualitative guidelines for calcified plaque, lipid and fibrous region identification. The wavelength dependence of optical attenuation of OCT signal was extracted for several regions of arterial tissues for better quantitative assessment of vulnerable plaque. These results suggest that the dependence of optical attenuation coefficient of the OCT signal on wavelength may provide new insights and help with vascular tissue differentiation. We anticipate that due to its high spatial resolution and new quantitative morphological identification methods, OCT will become an indispensable tool for cardiovascular diagnostics.

Acknowledgment. The authors acknowledge the financial support from National Research Council of Canada – Genomic and Health Initiative (Phase 4). The funders had no role in study design, data collection and analysis, decision to publish, or preparation of the manuscript.

References

1. Tearney G.J., Jang I.-K., Bouma B.E. Optical coherence tomography for imaging the vulnerable plaque. *J Biomed Opt* 2006; 11(2): 021002, http://dx.doi.org/10.1117/1.2192697.

2. Xu C., Schmitt J.M., Carlier S.G., Virmani R. Characterization of atherosclerosis plaques by measuring both backscattering and attenuation coefficients in optical coherence tomography. *J Biomed Opt* 2008; 13(3): 034003, http://dx.doi.org/10.1117/1.2927464.

3. Kubo T., Imanishi T., Takarada S., Kuroi A., Ueno S., Yamano T., Tanimoto T., Matsuo Y., Masho T., Kitabata H., Tsuda K., Tomobuchi Y., Akasaka T. Assessment of culprit lesion morphology in acute myocardial infarction: ability of optical coherence tomography compared with intravascular ultrasound and coronary angioscopy. *J Am Coll Cardiol* 2007; 50(10): 933–939, http://dx.doi.org/10.1016/j.jacc.2007.04.082.

4. Jang I.K, Tearney G.J., MacNeil B., Takano M., Moselewski F., Iftimia N., Shishkov M., Houser S., Aretz H.T., Halpern E.F., Bouma B.E. In vivo characterization of coronary atherosclerotic plaque by use of optical coherence tomography. *Circulation* 2005; 111(12): 1551–1555, http://dx.doi.org/10.1161/01.CIR.0000159354.43778.69.

5. Liu L., Gardecki J.A., Nadkarni S.K., Toussaint J.D., Yagi Y., Bouma B.E., Tearney G.J. Imaging the subcellular structure of human coronary atherosclerosis using micro-optical coherence tomography. *Nat Med* 2011; 17(8): 1010–1014, http://dx.doi.org/10.1038/nm.2409.

6. Yabushita H., Bouma B.E., Houser S.L., Aretz H.T., Jang I.-K., Schlendorf K.H., Kauffman C.R., Shishkov M., Kang D.-H., Halpern E.F., Tearney G.J. Characterization of human atherosclerosis by optical coherence tomography. *Circulation* 2002; 106(13): 1640–1645, http://dx.doi.org/10.1161/01.CIR.0000029927.92825.F6.

7. Jang I.-K., Bouma B.E., Kang D.-H., Park S.-J., Park S.-W., Seung K.-B., Choi K.-B., Shishkov M., Schlendorf K., Pomerantsev E., Houser S.L., Aretz H.T., Tearney G.J. Visualization of coronary atherosclerotic plaques in patients with optical coherence tomography: comparison with intravascular ultrasound. *J Am Coll Cardiol* 2002; 39(4): 604–609, http://dx.doi.org/10.1016/s0735-1097(01)01799-5.

8. Popescu D.P., Flueraru C., Mao Y., Chang S., Sowa M.G. Signal attenuation and box-counting fractal analysis of optical coherence tomography images of arterial tissue. *Biomed Opt Exp* 2010; 1(1): 268–277, http://dx.doi.org/10.1364/boe.1.000268.

9. Flueraru C., Popescu D.P., Mao Y., Chang S., Sowa M.G. Added soft tissue contrast using signal attenuation and the fractal dimension for optical coherence tomography images of porcine arterial tissue. *Phys Med Biol* 2010; 55: 2317–2331, http://dx.doi.org/10.1088/0031-9155/55/8/013.

10. Oldenburg A.L., Xu C., Boppart S.A. Spectroscopic optical coherence tomography and microscopy. *IEEE J Select Topics Quantum Electron* 2007; 13(6): 1629–1640, http://dx.doi.org/10.1109/jstqe.2007.910292.

11. Radosevich A.J., Rogers J.D., Turzhitsky V., Mutyal N.N., Yi J., Roy H.K., Backman V. Polarized enhanced

backscattering spectroscopy for characterization of biological tissues at subdiffusion length scales. *IEEE J Select Topics Quantum Electron* 2012; 18(4): 1313–1325, http://dx.doi.org/10.1109/jstqe.2011.2173659.

12. Jaedicke V., Agcaer S., Robles F.E., Steinert M., Jones D., Goebel S., Gerhardt N.C., Welp H., Hofmann M.R. Comparison of different metrics for analysis and visualization in spectroscopic optical coherence tomography. *Biomed Opt Exp* 2013; 4(12): 2945–2961, http://dx.doi.org/10.1364/BOE.4.002945.

13. Mao Y., Flueraru C., Chang S., Popescu D.P., Sowa M.G. Performance analysis of a swept-source optical coherence tomography system with a quadrature interferometer and optical amplification. *Opt Comm* 2011; 284(10–11): 2622–2627, http://dx.doi.org/10.1016/j.optcom.2011.01.016.

14. Mao Y., Flueraru C., Chang S., Popescu D.P., Sowa M.G. High-quality tissue imaging using a catheter-based swept-source optical coherence tomography system with an integrated semiconductor optical amplifier. *IEEE Trans on Instrum Measur* 2011; 60(10): 3376–3383, http://dx.doi.org/10.1109/tim.2011.2126950.

15. Flueraru C., Kumazaki H., Sherif S., Chang S., Mao Y. Quadrature Mach–Zehnder interferometer with application in optical coherence tomography. *J Optics A: Pure and Applied Optics* 2007; 9(4): L5–L8, http://dx.doi.org/10.1088/1464-4258/9/4/L01.

16. Flueraru C., Chang S., Sherif S. *Interferometric system for complex image extraction.* US Patent No.7,508,523. 2009.

17. Mao Y., Chang S., Sherif S., Flueraru C. Graded-index fiber lens proposed for ultrasmall probes used in biomedical imaging. *Appl Opt* 2007; 46(23): 5887–5894, http://dx.doi.org/10.1364/AO.46.005887.

18. Shiomi M., Ito T., Yamada S., Kawashima S., Fan J. Development of an animal model for spontaneous myocardial infarction (WHHLMI-rabbit). *Atheroscler Thromb Vasc Biol* 2003; 23(7): 1239–1244, http://dx.doi.org/10.1161/01.ATV.0000075947.28567.50.

19. Watanabe Y. Serial inbreeding of rabbits with hereditary hyperlipidemia (WHHL-rabbit). *Atherosclerosis* 1980; 36(2): 261–268, http://dx.doi.org/10.1016/0021-9150(80)90234-8.

20. Schmitt J.M., Knuttel A., Yadlowsky M., Eckhauss M.A. Optical coherence tomography of a dense tissue: statistics of attenuation and backscattering. *Phys Med Biol* 1994; 39(10): 1705–1720, http://dx.doi.org/10.1088/0031-9155/39/10/013.

21. Thrane L., Yura H.T., Andersen P.E. Analysis of optical coherence tomography systems based on the extended Huygens Fresnel principle. *J Opt Soc Am A* 2000; 17(3); 484–490, http://dx.doi.org/10.1364/JOSAA.17.000484.

22. Faber D., Van Der Meer F., Aalders M., van Leeuwen T. Quantitative measurement of attenuation coefficients of weakly scattering media using optical coherence tomography. *Opt Express* 2004; 12(19): 4353–4365, http://dx.doi.org/10.1364/OPEX.12.004353.

23. Turchin I.V., Sergeeva E.A., Dolin L.S., Kamensky V.A., Shakhova N.M., Richards-Kortum R. Novel algorithm of processing optical coherence tomography images for differentiation of biological tissue pathologies. *J Biomed Opt* 2005; 10(6): 064024, http://dx.doi.org/10.1117/1.2137670.

24. Turchin I.V., Sergeeva E.A., Dolin L.S., Kamensky V.A. Estimation of biotissue scattering properties from OCT images using a small-angle approximation of transport theory. *Laser Physics* 2003; 13(12): 1524–1529.

25. Morgner U., Drexler W., Kartner F.X., Li X.D., Pitris C., Ippen E.P., Fujimoto J.G. Spectroscopic optical coherence tomography. *Opt Lett* 2000; 25(2): 111–113, http://dx.doi.org/10.1364/ol.25.000111.

26. Leitgeb R., Wojtkowski M., Kowalczyk A., Hitzenberger C.K., Sticker M., Fecher A. Spectral measurement of absorption by spectroscopic frequency-domain optical coherence tomography. *Opt Lett* 2000; 25(11): 820–822, http://dx.doi.org/10.1364/ol.25.000820.

27. Robles F., Graf R.N., Wax A. Dual window method for processing spectroscopic optical coherence tomography signals with simultaneously high spectral and temporal resolution. *Opt Exp* 2009; 17(8): 6799–6812, http://dx.doi.org/10.1364/oe.17.006799.

28. Kraszewski M., Trojanowski M., Strakowski M.R. Quantitative comparison of analysis methods for spectroscopic optical coherence tomography: comment. *Biomed Opt Exp* 2014; 5(9): 3023–3033, http://dx.doi.org/10.1364/BOE.5.003023.

29. Bosschaart N., van Leeuwen T.G., Aalders M.C., Faber D.J. Quantitative comparison of analysis methods for spectroscopic optical coherence tomography: reply to comment. *Biomed Opt Exp* 2014; 5(9): 3034–3035, http://dx.doi.org/10.1364/boe.5.003034.

30. Prati F., Regar E., Mintz G.S., Arbustini E., Di Mario C., Jang I.-K., Akasaka T., Costa M., Guagliumi G., Grube E., Ozaki Y., Pinto F., Serruys P.W.J. Expert review document on methodology, terminology, and clinical applications of optical coherence tomography: physical principles, methodology of image acquisition, and clinical application for assessment of coronary arteries and atherosclerosis. *Eur Heart J* 2010; 31(4): 401–415, http://dx.doi.org/10.1093/eurheartj/ehp433.

31. Yonetsu T., Kakuta T., Lee T., Takahashi K., Kawaguchi N., Yamamoto G., Koura K., Hishikari K., Iesaka Y., Fujiwara H., Isobe M. In vivo critical fibrous cap thickness for rupture-prone coronary plaques assessed by optical coherence tomography. *Eur Heart J* 2011; 32(10): 1251–1259, http://dx.doi.org/10.1093/eurheartj/ehq518.